

# UC San Diego

## UC San Diego Previously Published Works

### Title

Cryo-electron Microscopy Reconstruction and Stability Studies of the Wild Type and the R432A Variant of Adeno-associated Virus Type 2 Reveal that Capsid Structural Stability Is a Major Factor in Genome Packaging

### Permalink

<https://escholarship.org/uc/item/10z4d48p>

### Journal

Journal of Virology, 90(19)

### ISSN

0022-538X

### Authors

Drouin, Lauren M

Lins, Bridget

Janssen, Maria

et al.

### Publication Date

2016-10-01

### DOI

10.1128/jvi.00575-16

Peer reviewed

# Cryo-electron Microscopy Reconstruction and Stability Studies of the Wild Type and the R432A Variant of Adeno-associated Virus Type 2 Reveal that Capsid Structural Stability Is a Major Factor in Genome Packaging

Lauren M. Drouin,<sup>a\*</sup> Bridget Lins,<sup>a\*</sup> Maria Janssen,<sup>c\*</sup> Antonette Bennett,<sup>a</sup> Paul Chipman,<sup>a</sup> Robert McKenna,<sup>a</sup> Weijun Chen,<sup>b</sup> Nicholas Muzyczka,<sup>b</sup> Giovanni Cardone,<sup>c\*</sup> Timothy S. Baker,<sup>c</sup> Mavis Agbandje-McKenna<sup>a</sup>

Department of Biochemistry and Molecular Biology, Center for Structural Biology, The McKnight Brain Institute, College of Medicine, University of Florida, Gainesville, Florida, USA<sup>a</sup>; Department of Molecular Genetics and Microbiology, University of Florida Genetics Institute, College of Medicine, University of Florida, Gainesville, Florida, USA<sup>b</sup>; Department of Chemistry and Biochemistry and Division of Biological Sciences, University of California—San Diego, San Diego, California, USA<sup>c</sup>

## ABSTRACT

The adeno-associated viruses (AAV) are promising therapeutic gene delivery vectors and better understanding of their capsid assembly and genome packaging mechanism is needed for improved vector production. Empty AAV capsids assemble in the nucleus prior to genome packaging by virally encoded Rep proteins. To elucidate the capsid determinants of this process, structural differences between wild-type (wt) AAV2 and a packaging deficient variant, AAV2-R432A, were examined using cryo-electron microscopy and three-dimensional image reconstruction both at an  $\sim 5.0$ -Å resolution (medium) and also at 3.8- and 3.7-Å resolutions (high), respectively. The high resolution structures showed that removal of the arginine side chain in AAV2-R432A eliminated hydrogen bonding interactions, resulting in altered intramolecular and intermolecular interactions propagated from under the 3-fold axis toward the 5-fold channel. Consistent with these observations, differential scanning calorimetry showed an  $\sim 10^\circ\text{C}$  decrease in thermal stability for AAV2-R432A compared to wt-AAV2. In addition, the medium resolution structures revealed differences in the juxtaposition of the less ordered, N-terminal region of their capsid proteins, VP1/2/3. A structural rearrangement in AAV2-R432A repositioned the  $\beta\text{A}$  strand region under the icosahedral 2-fold axis rather than antiparallel to the  $\beta\text{B}$  strand, eliminating many intramolecular interactions. Thus, a single amino acid substitution can significantly alter the AAV capsid integrity to the extent of reducing its stability and possibly rendering it unable to tolerate the stress of genome packaging. Furthermore, the data show that the 2-, 3-, and 5-fold regions of the capsid contributed to producing the packaging defect and highlight a tight connection between the entire capsid in maintaining packaging efficiency.

## IMPORTANCE

The mechanism of AAV genome packaging is still poorly understood, particularly with respect to the capsid determinants of the required capsid-Rep interaction. Understanding this mechanism may aid in the improvement of AAV packaging efficiency, which is currently  $\sim 1:10$  (10%) genome packaged to empty capsid in vector preparations. This report identifies regions of the AAV capsid that play roles in genome packaging and that may be important for Rep recognition. It also demonstrates the need to maintain capsid stability for the success of this process. This information is important for efforts to improve AAV genome packaging and will also inform the engineering of AAV capsid variants for improved tropism, specific tissue targeting, and host antibody escape by defining amino acids that cannot be altered without detriment to infectious vector production.

The adeno-associated viruses (AAVs) have emerged as attractive gene therapy vectors because they can package foreign genes and achieve stable, long-term gene expression in a broad range of tissues, with no known pathogenicity (1–3). AAVs are small, nonenveloped, icosahedral viruses ( $\sim 260$  Å in diameter) that package  $\sim 4.7$  kb of single-stranded DNA (ssDNA) (4). This genome contains the *rep*, *cap*, and *aap* open reading frames (ORFs) flanked by inverted terminal repeats of  $\sim 145$  bp. The *rep* gene expresses four nonstructural proteins (Rep78, Rep68, Rep52, and Rep40) required for viral replication and genome packaging. Three overlapping structural proteins (VP1, VP2, and VP3) share a VP3 region and are encoded by the *cap* gene. The unique N-terminal region of VP1 (VP1u) contains a phospholipase A2 domain, and the VP1u and VP1/2 common regions contain nuclear localization signals (NLS). The PLA2 and NLS are required for viral infection (5, 6). Sixty VPs form the T=1 viral capsid in a VP1/VP2/VP3 ratio of 1:1:10 (7–10). The more recently identified *aap*

ORF encodes the assembly-activating protein, which is necessary for capsid assembly (11–13).

The AAV VP3 common structure is comprised of a  $\beta\text{A}$  strand, an eight-stranded  $\beta$ -barrel core ( $\beta\text{B}$ - $\beta\text{I}$ ), and a small  $\alpha$ -helix ( $\alpha\text{A}$ ), which are conserved in all parvovirus structures, and contain large loop insertions that link these secondary structure elements and are located on the capsid surface (14–23). The tops of these insertion loops are classified into nine major variable regions (VRs) that vary in sequence and structure among the different serotypes. These VRs are associated with specific functional roles, including receptor attachment, transduction phenotype, and antigenicity, for each of the AAV serotypes (15, 24–34). The VPs assemble a capsid whose morphology is characterized by surface depressions at the icosahedral 2-fold axes of symmetry, three protrusions surrounding a depression at each 3-fold axis, and a pore at each 5-fold axis surrounded by a shallow (canyon-like) depression (14–23).

AAVs package their ssDNA genomes into preformed capsids through the use of Rep (35–39). The current model for packaging is that (i) empty capsids assemble in the nucleoli and then associate with Rep52 and Rep78 complexes; (ii) Rep78/68 proteins associate with the 5' end of the AAV genome to be packaged, which is then docked onto the preexisting Rep-capsid complex; and (iii) the helicase activities of both Rep proteins load the ssDNA into the capsid in a 3' to 5' direction. However, exactly how these processes occur is poorly understood and the capsid determinants of successful genome packaging are not well characterized.

In a charge-to-alanine mutagenesis screen of AAV2, a single residue change, R432A, was identified as having a severe genome-packaging defect (a 5-log decrease) compared to wild-type AAV2 (wt-AAV2) (34). This residue is buried within the capsid at a 3-fold symmetric VP-VP interface. This site is not accessible from the exterior surface of the capsid, where it could potentially interact with Rep, nor is it accessible from the interior surface of the capsid, where it could interact with the packaged DNA. Thus, the role of residue 432 in genome packaging is difficult to reconcile. Further studies of AAV2-R432A reported an indirect effect on packaging due to tighter association with Rep52 and Rep78 compared to wt-AAV2 rather than a lack of interaction with the packaging machinery (40). AAV2-R432A was also reported to have its VP1 and VP2 N termini abnormally exposed on the capsid surface at room temperature, in contrast to wt-AAV2 (37). Based on these observations, it was postulated that the VP N termini of AAV2-R432A are extruded through the 5-fold pores, one of which is proposed to be the portal for genome packaging in parvoviruses (6, 35, 40, 41), thus blocking the route for DNA encapsulation. However, chimeric AAV2 variants with externalized VP1 and VP2 still maintain wt packaging efficiencies (5, 42, 43). Therefore, if the 5-fold channel indeed functions as the packaging portal, perhaps not all 12 channels are blocked by extruded N termini, and this might suggest that a different mechanism of action occurs in AAV2-R432A. It is noteworthy that a second residue in AAV2, R513, which when mutated to alanine also abrogates DNA packaging, is located close to R432 from a 3-fold related VP monomer (44). These observations suggest a role for the 3-fold interface interactions in genome packaging and possibly Rep association.

In this report, the structures of wt-AAV2 and AAV2-R432A virus-like particles (VLPs) produced in a baculovirus/sf9 system

were determined by cryo-electron microscopy (cryo-EM) and three-dimensional (3D) image reconstruction (cryo-EM reconstruction) to ~3.8- and ~3.7-Å resolutions, respectively. The R432A mutation resulted in a loss of intra- and inter-VP monomer interactions, as well as conformational side- and main-chain rearrangements propagated from the 3-fold region to the base of the 5-fold channel. We also compared the wt and AAV2-R432A structures studied at ~5.0-Å resolution. This enabled the visualization and interpretation of less well-ordered VP features that are not visible in the higher resolution cryo-EM reconstruction owing to signal loss at high spatial frequency. A striking difference was observed in the repositioning of the  $\beta$ A strand in AAV2-R432A compared to wt-AAV2. In AAV2-R432A, residues within this strand are repositioned near the 2-fold axis, which is distinct from its antiparallel pairing with strand  $\beta$ B in the capsid interior of wt-AAV2. Consistent with the loss of side chain and interface interactions in AAV2-R432A, analysis of capsid stability using differential scanning calorimetry (DSC) showed an ~10°C decrease in thermostability. Overall, the observations indicate that residues at the 2-, 3-, and 5-fold interface regions of the capsid must maintain a certain topology in addition to interactions that control Rep binding and confer a level of capsid stability sufficient for ssDNA packaging to occur.

## MATERIALS AND METHODS

**Generation of wt-AAV2 and AAV2-R432A baculovirus constructs.** The pFBDVPm11 baculovirus donor plasmid (45), containing a mutation in the AAV2 *cap* start site to ensure that correct ratios of VP1, VP2, and VP3 are expressed (a generous gift from Sergei Zolotukhin, Department of Pediatrics, University of Florida), was used for the generation of the baculovirus construct for AAV2-R432A. To insert the R432A mutation into the *cap* gene, the pFBDVPm11 and available pIM45-AAV2-R432A (34) plasmids were double digested with the XcmI and BsiWI restriction enzymes (New England BioLabs), and the appropriate DNA fragments were excised from an agarose gel and purified. The purified vector (pFBDVPm11) and insert (AAV2-R432A) DNA were ligated between the BsiWI and XcmI restriction endonuclease sites in a 1:2 ratio, and the resultant plasmid was used to transform JM109 electrocompetent cells (Stratagene). The resulting colonies were grown overnight, followed by plasmid DNA purification using a MiniPrep kit (Qiagen). The isolates were digested with BsiWI and electrophoresed on an agarose gel to confirm the presence of the AAV2-R432A insert, and one positive isolate was selected for DNA sequencing using AAV2 *cap*-specific primers.

The original pFBDVPm11 and pFBDVPm11-AAV2-R432A donor plasmids were used to generate recombinant baculovirus according to the manufacturer's specifications (Invitrogen Bac-to-Bac baculovirus expression system). Individual baculovirus clones were amplified in *Spodoptera frugiperda* (Sf9) cells maintained in Sf900 II SFM media (Gibco) and supplemented with 1% antibiotic-antimycotic (Gibco). The resulting clones were plaque purified and amplified to the P1 stage (passage 1) and then assayed for VP production by Western blotting. The titers of the highest-producing clones were determined by plaque assay, and these clones were then amplified to produce P2 stocks. In turn, the titers of the P2 stocks were determined, and the clone with the highest concentration was amplified to produce a P3 stock. The titer of this P3 stock was also determined, and this stock was then used for VLP production.

**Large-scale expression and purification of wt-AAV2 and AAV2-R432A VLPs.** The P3 stocks of the wt-AAV2 and AAV2-R432A baculovirus constructs were used to infect 1 liter of Sf9 cells ( $2 \times 10^6$  cells/ml) in suspension at 27°C with a multiplicity of infection of 5. The infected cells were harvested 72 h postinfection and centrifuged at 3,000 rpm in a JS-5.3 rotor for 15 min to produce a pellet. The cell pellet was resuspended in lysis buffer (137 mM NaCl, 0.7 mM Na<sub>2</sub>HPO<sub>4</sub>, 5 mM KCl, and 25 mM

Received 27 March 2016 Accepted 12 July 2016

Accepted manuscript posted online 20 July 2016

**Citation** Drouin LM, Lins B, Janssen M, Bennett A, Chipman P, McKenna R, Chen W, Muzyczka N, Cardone G, Baker TS, Agbandje-Mckenna M. 2016. Cryo-electron microscopy reconstruction and stability studies of the wild type and the R432A variant of adeno-associated virus type 2 reveal that capsid structural stability is a major factor in genome packaging. *J Virol* 90:8542–8551. doi:10.1128/JVI.00575-16.

**Editor:** L. Banks, International Centre for Genetic Engineering and Biotechnology

Address correspondence to Timothy S. Baker, tsb@ucsd.edu, or Mavis Agbandje-Mckenna, mckenna@ufl.edu.

L.M.D., B.L., and M.J. contributed equally to this article.

\* Present address: Lauren M. Drouin, Voyager Therapeutics, Inc., Cambridge, Massachusetts, USA; Bridget Lins, Division of Viral Products, CBER/FDA, Silver Spring, Maryland, USA; Maria Janssen, The Scripps Research Institute, La Jolla, California, USA; Giovanni Cardone, The Facility of Optical Imaging, Max Planck Institute of Biochemistry, Martinsried, Germany.

Copyright © 2016, American Society for Microbiology. All Rights Reserved.

Tris-HCl [pH 7.4] plus 0.2% Triton X-100) in the presence of protease inhibitor (Roche) and subjected to three cycles of rapid freezing and thawing. Benzoylase (Sigma-Aldrich) was added to the sample after the final thaw, followed by incubation at 37°C for 30 min, with periodic vortexing. The crude cell lysate was clarified by centrifugation in a JA-20 rotor at 9,000 rpm for 20 min, and the supernatant was collected.

The supernatant was purified using an iodixanol step gradient (OptiPrep medium; Sigma-Aldrich) in 32.4-ml OptiSeal tubes (Beckman Coulter). Samples were layered on top of the gradient tubes and centrifuged at 59,000 rpm for 2 h in a 60 Ti rotor at 18°C. Fractions were collected from the bottom of the tube by needle puncture and dripping into collection tubes. Each fraction was further purified by anion exchange using a 5-ml prepacked HiTrap Q HP column (GE Healthcare) on an AKTA FPLC/Unicorn system (GE Healthcare). After washing with 20 mM Tris-HCl (pH 8.5)–15 mM NaCl, 1-ml fractions were eluted with a linear gradient of 20 mM Tris-HCl (pH 8.5)–500 mM NaCl.

The fractions were monitored for the presence of the wt-AAV2 and AAV2-R432A VPs (VP1 [87 kDa], VP2 [72 kDa], and VP3 [62 kDa]) by SDS-PAGE using 4 to 15% Criterion TGX precast gels (Bio-Rad) that were stained with Bio-Safe Coomassie stain (Bio-Rad). The specificity of the visualized VP bands and the presence of assembled capsids were verified by Western and native dot blot analyses, respectively, using the B1 and A20 or C37-B antibodies (33), respectively. The integrity of the purified VLPs was confirmed by negative-stain (2% uranyl acetate) electron microscopy using an FEI Spirit transmission electron microscope (TEM) operating at 120 kV. The micrographs were collected using a Gatan 2Kx2K charged-coupled device camera.

**Cryo-EM.** Cryo-electron micrographs were recorded from wt-AAV2 and AAV2-R432A samples vitrified on Quantifoil grids using an FEI Polara microscope. Small aliquots (3.5  $\mu$ l) of each sample, at  $\sim$ 1 mg/ml, were applied to glow-discharged, holey Quantifoil grids and vitrified by manual plunging into liquid ethane. The grids were transferred into a precooled FEI Polara multispecimen holder, which maintained the specimen at liquid nitrogen temperature. Cryo-EM images were recorded on Kodak SO163 films under low-dose conditions ( $\sim$ 20  $e^-/\text{\AA}^2$ ) at 1.1 to 3.7  $\mu$ m and 1.2 to 3.2  $\mu$ m under focus for wt-AAV2 and AAV2-R432A, respectively, on an FEI Tecnai G2 (Polara) TEM operated at 300 kV and a nominal magnification of  $\times$ 59,000 with parallel beam illumination. Micrographs were digitized on a Nikon Super Coolscan 8000 microdensitometer scanner at 6.35- $\mu$ m intervals (representing 1.12  $\text{\AA}$  pixels at the specimen level) and saved in the PIF format for further processing and structure determination.

**Data processing and 3D image reconstruction.** For both data sets, the application CTFIND (46) within the AUTO3DEM software package (47) (<http://cryoem.ucsd.edu/programs.shtm>) was used to determine the defocus value and astigmatism parameters for each micrograph. Micrographs that exhibited minimal astigmatism and specimen drift were selected for further processing. The RobEM subprogram in AUTO3DEM was used to extract individual particle images and to preprocess them as described previously (48). The random-model computation procedure (49) was used to generate an initial reconstructed model at  $\sim$ 25- $\text{\AA}$  resolution from 150 particle images. This map was used to initiate full determination of the orientations and origins of all particles and refinement of the entire set of images utilizing AUTO3DEM (47). To reduce noise, the maps were masked during alignment procedures. The microscope contrast transfer function (CTF) was refined using AUTO3DEM for each image. The phases but not the amplitudes of the structure factor data were corrected for effects caused by the CTF prior to the final map calculation.

The wt-AAV2 data included in the final cryo-EM reconstruction consisted of 23,039 particle images selected from 64 micrographs. The 3D map was estimated to be reliable to at least a 3.8- $\text{\AA}$  resolution (Fourier shell correlation [FSC] threshold = 0.5) (50). The AAV2-R432A data set consisted of 19,457 particle images selected from 49 micrographs, which yielded a final 3D map that was estimated to be reliable to at least 3.7- $\text{\AA}$  resolution (FSC = 0.5). Maps were computed with inverse temperature

factors (51) of 1/150  $\text{\AA}^2$  and 1/100  $\text{\AA}^2$  for the wt-AAV2 and AAV2-R432A structures, respectively, to enhance the higher spatial frequency details. These values were empirically determined by screening a range of values from 1/50 to 1/500  $\text{\AA}^2$ . For both structures, the Fourier amplitudes were multiplied by a noise suppression factor to filter out spatial frequencies in the map according to FSC resolution estimates to prevent excessive amplification of noise. In addition to the final high-resolution maps, density maps at the medium resolution of 5.0  $\text{\AA}$ , generated in earlier steps of the structure determination process, were utilized for comparative analyses of less well-ordered VP features. A 60mer coordinate file was generated from the AAV2 VP crystal structure (PDB 1LP3) with the Oligomer Generator subroutine in VIPERdb (52) and docked into the high- and medium-resolution wt-AAV2 and AAV2-R432A maps using the Chimera program (53) to determine the absolute hand of each map prior to comparative analysis.

**Comparison of cryo-EM reconstructed density maps, model building, and model refinement.** The 3D density maps were normalized and visualized in Chimera at a density threshold of 1.0  $\sigma$  for analysis and interpretation. Model building into the wt-AAV2 and AAV2-R432A maps was performed using the program COOT (54). This procedure made use of the available AAV2 crystal structure coordinates (PDB 1LP3) as a template and was guided by the cryo-reconstructed maps. Each of the resulting VP monomer models was utilized to generate a 60mer capsid model, as described above, and refined against the high resolution cryo-reconstructed maps using the newly developed “Real-space Refinement” subroutine within the PHENIX program (55). The refined models were compared to each other and the AAV2 crystal structure in COOT (54). The figures were generated using the PyMOL (56) and Chimera (53) programs.

**Differential scanning calorimetry.** wt-AAV2 and AAV2-R432A VLPs, purified from the 25/40% and 40% iodixanol fractions, respectively, were dialyzed into 1 $\times$  phosphate-buffered saline (PBS; pH 7.4), using 150-kDa nominal cutoff Apollo concentrators (Orbital Biosciences) to characterize capsid stability. Approximately 0.5 ml of wt-AAV2 at 0.3 mg/ml, AAV2-R432A at 0.4 mg/ml, and 1 $\times$  PBS (pH 7.4; as the reference buffer) were subjected to heating from 10 to 100°C at a scan rate of 60°C/h in a MicroCal VP-DSC instrument (GE Healthcare). The reference buffer and samples were loaded into two separate chambers for comparison, and each experiment was conducted in triplicate. The data obtained from the three thermal scans were plotted, normalized, and analyzed using the Origin software suite (OriginLab). The melting temperatures from each scan were averaged to improve the signal-to-noise ratio, and the standard deviations were calculated to provide error values.

**Accession number(s).** The wt-AAV2 and AAV2-R432A density maps and models built into the maps have been deposited at the EMDB database as data set EMD-8099 and PDB 5IPI and data set EMD-8100 and PDB 5IPK, respectively.

## RESULTS

**Structures of wt-AAV2 and AAV2-R432A.** Analysis of purified VLPs by SDS-PAGE, Western and native dot blots, and negative-stain EM showed that the wt-AAV2 and AAV2-R432A baculovirus constructs were both capable of producing pure intact particles suitable for structural analysis (data not shown). These samples were vitrified and used to generate cryo-reconstructed structures at two different resolutions: 5.0/3.8  $\text{\AA}$  for wt-AAV2 and 5.0/3.7  $\text{\AA}$  for AAV2-R432A (Fig. 1). Comparison of the maps for each virus showed an increase in structural detail of the capsid surface features with increasing resolution, as expected. All maps clearly showed the characteristic features of an AAV capsid: a depression at each 2-fold axis and surrounding each 5-fold axis, and three protrusions surrounding each 3-fold axis (Fig. 1). The density for the HI (between  $\beta$ -strands H and I) and DE (between  $\beta$ -strands D and E) loops were also clearly defined (Fig. 1).



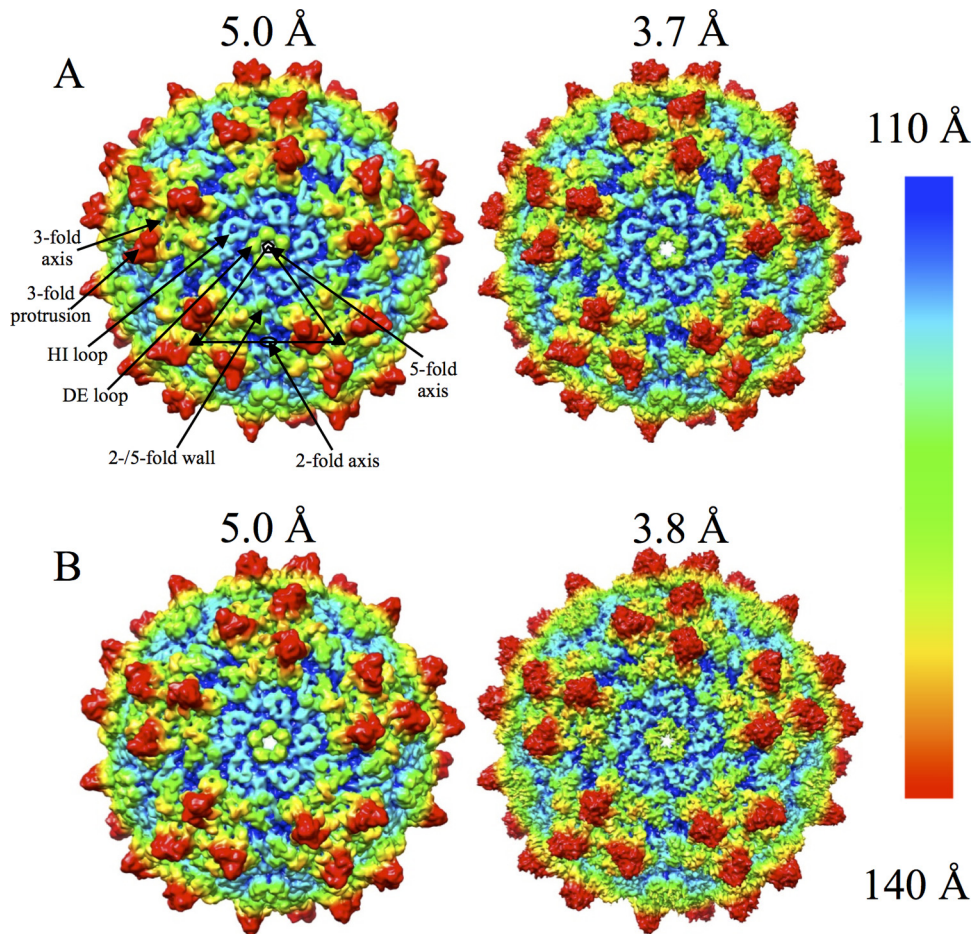


**FIG 1** Cryo-EM reconstructions of wt-AAV2 and AAV2-R432A. Radially colored AAV2-R432A (A) and wt-AAV2 (B) density maps at medium ( $\sim 5.0$  Å) and high (3.7/3.8 Å) resolutions, respectively. A viral asymmetric unit is delineated by the triangle on the capsid surface of the medium-resolution AAV2-R432A map in panel A. The positions of select 2-, 3-, and 5-fold axes are indicated by oval, triangle, and pentagon symbols, respectively. The positions of an HI loop, a DE loop, a 3-fold protrusion, and the 2-/5-fold wall are indicated. The density in panels A and B are shown at a sigma threshold of 1.0.

Amino acid side chains were clearly represented in the wt-AAV2 and AAV2-R432A high-resolution maps (Fig. 2A). Residues 225 to 735 (VP1 numbering) and 236 to 735 (here referred to as VP3) were interpretable in the wt-AAV2 and AAV2-R432A maps, respectively. The correlation coefficients for the real-space refinement of the models were 0.71 (wt-AAV2) and 0.73 (AAV2-R432A). The lack of ordering of the VP1u, VP1/2 common region, and first 22/33 residues of VP3 is consistent with previous AAV structure reports (57). The observation is predicted to be due to low copies of VP1 and VP2 within the capsid and conformational variation of the overlapping VP1/2/3 N termini. The models built into the wt-AAV2 and AAV2-R432A cryo-EM reconstructed density maps superpose with a root mean square deviation (RMSD) of 0.93 Å (Fig. 2B). The wt-AAV2 VP model built into the 3.8-Å structure superposed onto the available AAV2 crystal structure with an RMSD of 1.25 Å. Differences were observed at the top of the 3-fold protrusions, notably within VRs IV and V (not shown). The AAV2-R432A VP model superposed onto the AAV2 crystal structure with an RMSD of 1.13 Å.

**Comparison of AAV2-R432A to wt-AAV2 reveals differences at high and medium resolutions.** A residue level comparison of the VP3 models built onto the high-resolution maps showed the

ordered R432 side chain in the wt-AAV2 map, which was absent in AAV2-R432A, a finding consistent with the genome mutation (Fig. 2B and 3A). In addition, other changes occurred in the immediate vicinity of residue A432, along with some at distant positions. Immediately adjacent to A432, the side chains for D431 and R513 are also disordered (Fig. 3). In the wt-AAV2 structure, the capsid is stabilized by polar interactions between the guanidine group of R432 on the reference VP monomer and the main-chain carbonyl oxygens of D269 and H271 of a 3-fold-related monomer. Residues 269 and 271 are situated within a surface loop located on the 2/5-fold wall of the capsid (Fig. 3A). In addition, the epsilon nitrogen of R432 participates in a polar interaction with one of the oxygen atoms of the carboxyl group of D431 on the same VP monomer. The D431 carboxyl group oxygen also interacts with the guanidine group of R513 on the 3-fold related VP monomer (Fig. 3A). These interactions do not occur in AAV2-R432A owing to side chain conformational changes/disorder in D431 and R513, likely arising from the lack of stabilization from the side chain of R432. Although residue 432 and the disrupted contacts with residues 431 and 513 are buried within the capsid, surface differences immediately above residue 432 occur at R471 and W502 (Fig. 3B and 4). Arginine 471 of the reference monomer is disordered in

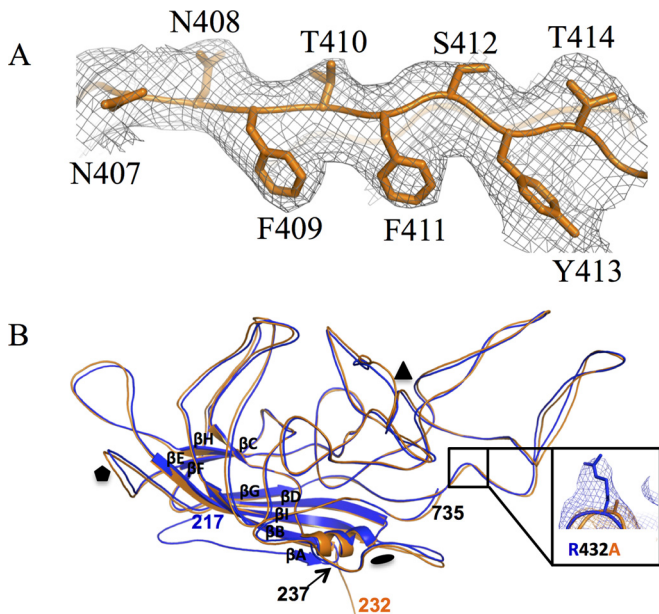


**FIG 2** Density map and model of AAV2-R432A. (A) Small region of the AAV2-R432A cryo-EM density map (gray mesh) with modeled residues 407 to 414. These residues were readily interpretable in the map. (B) Superposition of the AAV2-R432A (orange) and wt-AAV2 (blue) ribbon models built into the cryo-reconstructed density maps. The enlarged inset image shows the location and orientation of residue 432 in the wt-AAV2 (blue mesh) and AAV2-R432A (orange mesh) density maps. The densities in panels A and B are shown at a sigma threshold of 2.0.

wt-AAV2 but becomes ordered in AAV2-R432A, which is concomitant with a shift in the side chain of W502 of the 3-fold-related monomer that appears to stabilize R471 (Fig. 3B). These two side chain shifts are the only surface-exposed conformational changes in the AAV2-R432A structure and are located immediately adjacent to the side chain of D269 at the base of the protrusions surrounding the 3-fold axes on the wall facing the 5-fold axis (Fig. 4).

The substitution of an alanine for an arginine at position 432 propagates changes in two VP regions that are far from the mutated residue in the AAV2-R432A structure. One of these occurs in the conserved  $\beta$ A strand of VP3. In the AAV2-R432A map, the first ordered residue is 236, which is 11 and 19 amino acids upstream from that observed in the wt-AAV2 structure determined in this study and that in the previously determined AAV2 crystal structure, respectively (Fig. 5). Thus, maps at a lower resolution (5.0 Å) generated from fewer particle images were analyzed in an effort to visualize the less-ordered VP features of the capsid because the signal for less structurally ordered regions of macromolecules (or components of complexes with a reduced copy number) can be lost at high resolution. This is due to the finer spatial frequency of data sampling which can be overcome at lower resolution. Models built into these low resolution maps showed the main chain of VP3 to be traceable, and the BIDG and CHEF  $\beta$  sheets, as well as the  $\alpha$ A helix, were visible, but side chain densities were not resolved (not shown). The AAV2-R432A map showed a buildup of density projecting into the capsid interior from residue 236 (located on the interior surface) and at the 2-fold symmetry axis (Fig. 6A). The main chain for four additional residues could be modeled into this 5.0-Å density map, extending the AAV2-

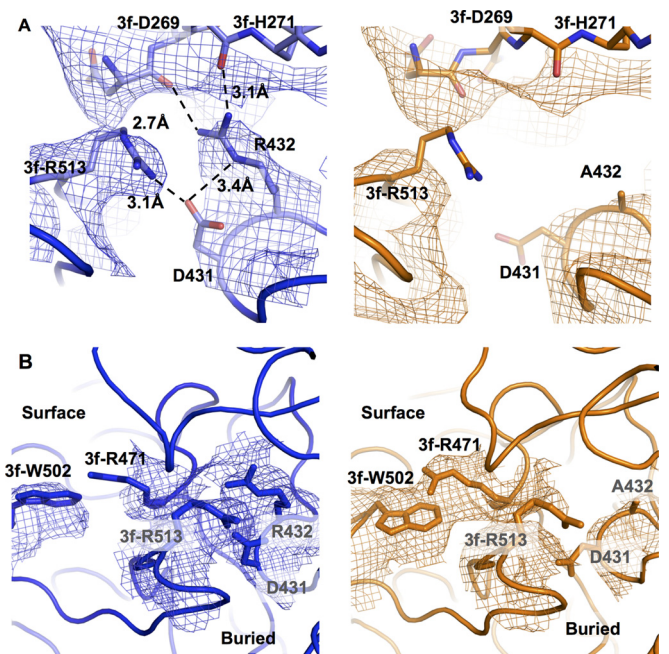


**FIG 3** Residue level structural rearrangements in AAV2-R432A. (A) Intra- and inter-VP monomer interactions in wt-AAV2 structure (blue density mesh and model) between R432 (on the reference VP monomer) with D431 (on the same VP monomer), with 3f-D269 and 3f-H271 (of a 3-fold-related monomer), which likely serve to stabilize the native capsid, are lost in AAV2-R432A (orange density mesh and model). In this vicinity the interaction between D431 with 3f-R513 in wt-AAV2 is absent in AAV2-R432A. The loss of interactions in AAV2-R432A is due to the lack of the arginine side chain in A432 and side chain conformational changes/disorder in D431 and R513. (B) Surface differences between wt-AAV2 and AAV2-R432A at positions R471 and W502 located above D431, R432, and R513. R471 is disordered in wt-AAV2 but ordered in AAV2-R432A, concomitant with a shift in the side chain of W502 of the 3-fold-related monomer. The densities in panels A and B are shown at a sigma threshold of 1.5.

R432A VP3 chain to N-terminal residue 232 (Fig. 6B). However, this main chain is rotated  $\sim 60^\circ$  toward the 2-fold rather than extending toward the 5-fold axis as in the wt-AAV2 cryo-reconstructed and crystal structures (Fig. 2B and 6B). In the wt-AAV2 map, additional density is observed in the interior surface at the 3-fold axis, which is absent in the AAV2-R432A map (Fig. 6A). This additional density is proximal to but does not overlap with the position of the nucleotide density observed in the capsid interior of the majority of other wt-AAV serotype capsid structures determined to date (58). While a nucleotide model was not built into this 3-fold density, its absence in the AAV2-R432A is consistent with its DNA packaging defect.

The second VP site that differs far away from R432A in the AAV2-R432A structure is residue R404 located at the interior capsid opening of the 5-fold channel (Fig. 7A). This residue undergoes a rearrangement which positions the terminal amino groups of its side chain away from the opening of the channel (Fig. 7A). In the wt-AAV2 cryo-reconstructed structure, the first ordered residue, 225, is positioned immediately adjacent to R404 from a 5-fold-related VP (Fig. 7B). The reorganization of the  $\beta$ A strand and N terminus toward the 2-fold axis in AAV2-R432A creates a space that the R404 side chain occupies. Of note, an AAV2 R404A variant has been shown to produce a 14-fold reduction in DNA packaging (unpublished data).



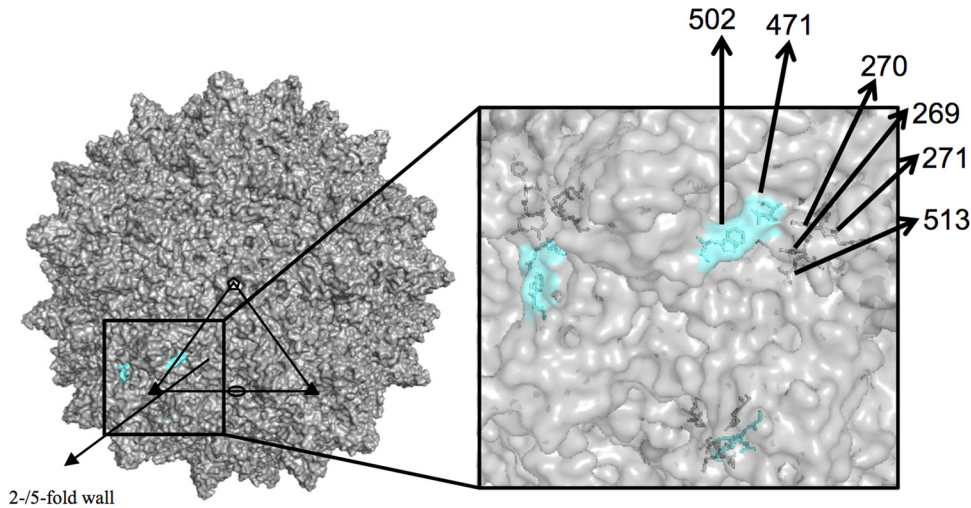


**FIG 4** Location of capsid surface differences between wt-AAV2 and AAV2-R432A. R471 and W502 are highlighted in cyan at the base of the 3-fold protrusion on the 2-/5-fold wall. Residues 269 to 271, which participate in main-chain interactions with R432A, and R513 (side chain interactions in wt-AAV2) are also highlighted. The densities in panels A and B are shown at a sigma threshold of 1.0.

**Wild-type and AAV2-R432A capsid stability.** The loss of interface interactions suggested that AAV2-R432A would be less stable than wt-AAV2. Differential scanning calorimetry was thus used to measure the thermostability of AAV2-R432A for comparison with wt-AAV2. The melting temperature ( $T_m$ ) determined for wt-AAV2 at pH 7.4 was  $67.5 \pm 0.3^\circ\text{C}$  and the native capsid exhibited a melting profile with a single, sharp denaturation peak (Fig. 8). This observation is congruent with a previously reported  $T_m$  of  $67.8 \pm 0.2^\circ\text{C}$  (59). In contrast, the AAV2-R432A melting

profile exhibited a “shoulder” prior to the major peak, resulting in two melting temperatures: peak 1 =  $57.5 \pm 0.2^\circ\text{C}$  and peak 2 =  $61.1 \pm 1.9^\circ\text{C}$  (Fig. 8). This dual melting profile suggests a two-step denaturation process for the mutant, which was not observed for wt-AAV2.

## DISCUSSION

Cryo-EM and image reconstruction yielding medium and high-resolution structures of wt-AAV2 and the packaging deficient variant AAV2-R432A revealed capsid properties required for genome encapsulation to occur. At 3.8 and 3.7 Å, respectively, these structures are among the highest-resolution structures determined to date of viruses with T=1 capsids using this experimental approach. With the high-resolution density maps, models of the wt-AAV2 and AAV2-R432A structures could be built using the known AAV2 crystal structure coordinates as a template. A comparison of these models showed an overall conservation of the VP3 monomer backbone structure. Side chain and main-chain differences visualized the altered capsid interactions inhibiting genome packaging. Significantly, the change at R432A, situated at a 3-fold VP:VP interface, showed structural changes that propagate to regions of the capsid near the 2- and 5-fold axes. Density maps at 5.0-Å resolution showed a large, main-chain rearrangement in AAV2-R432A that alters the juxtaposition of residues under the 5-fold and 2-fold axes. The data demonstrate that alterations at the 2-, 3-, and 5-fold regions of the capsid contribute to producing a packaging defect and highlight a tight connection between the entire capsid in maintaining packaging efficiency.

Sequence analysis of the VP3 of several AAV serotypes (AAV1-AAV9) indicated that R432 and the surrounding region (including D431) are highly conserved, AAV5 being the only exception (not shown). Amino acids W502 and R513 are also highly conserved among these AAVs, except in AAV4, which contains no structurally equivalent residue to position 502, and in AAV5, which contains F489 and A500, respectively. Residues 511-NGR-513, conserved in AAV1 to AAV13, except in AAV4, AAV5, and AAV11, form a partially exposed, capsid surface loop at the base of the 3-fold protrusions on the side facing the 2-fold depression.

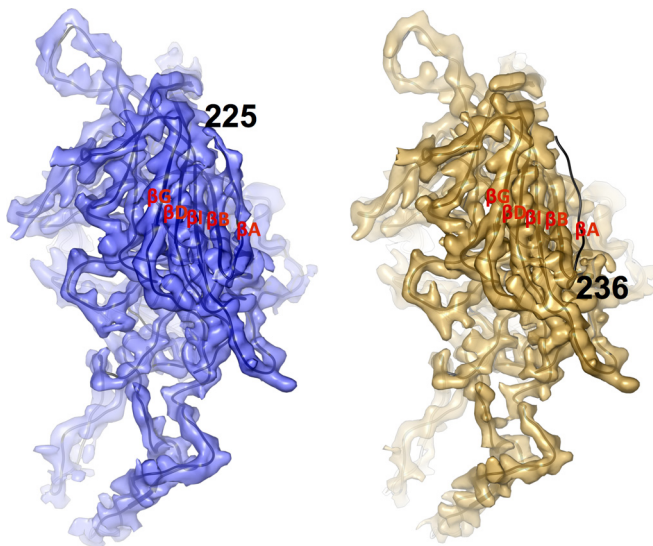


**FIG 5** Wild-type and AAV2-R432A N-terminal differences at high resolution. Density maps of wt-AAV2 (blue) and AAV2-R432A (orange) monomers viewed from the capsid interior are shown with the docked main chain (black line) of the AAV2 crystal structure coordinates (1LP3). Densities for the  $\beta$ B,  $\beta$ I,  $\beta$ D, and  $\beta$ G strands are well-ordered (labeled) and structurally equivalent in wt-AAV2 and AAV2-R432A, but the  $\beta$ A strand is absent in the AAV2-R432A density map. The interpretable density for the wt-AAV2 structure is ordered starting at residue 225, whereas the AAV2-R432A map only reveals the density starting at residue 236. The densities in panels A and B are shown at a sigma threshold of 2.5.

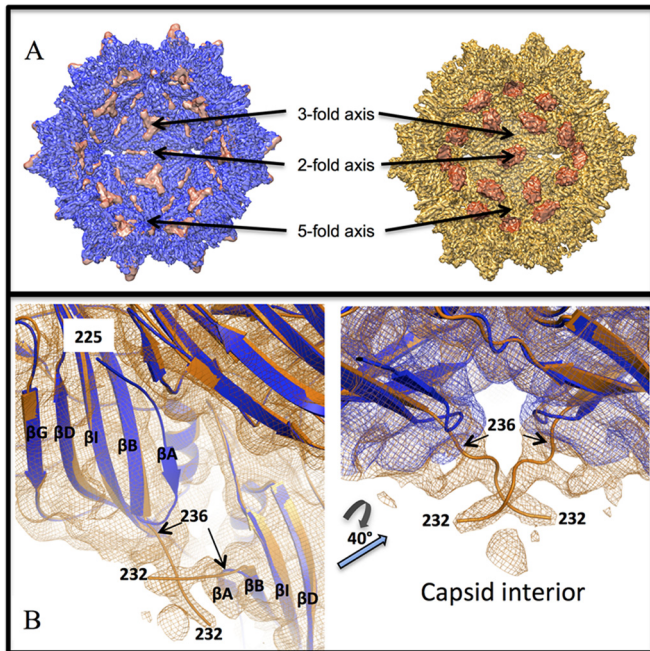


**FIG 6** Wild-type AAV2 and AAV2-R432A structural changes at the 2-fold symmetry axis seen at medium resolution. (A) Cross-section of the wt-AAV2 (left, blue) and AAV2-R432A (right, orange) capsid density maps showing positive difference density (cryo-reconstructed density minus AAV2 crystal structure capsid model density) primarily confined to the interior capsid surface. In wt-AAV2, extra density occurs at the 3-fold axes, whereas in AAV2-R432A, extra density occurs at the 2-fold axes. (B) Ribbon representations of a VP3 monomer fitted within the AAV2-R432A density map (orange) (left) and superposed wt-AAV2 (blue) and AAV2-R432A (orange) surface densities (right) close to the 2-fold axis. The  $\beta$ BID strands, as well as strand  $\beta$ A, are labeled in the left side of panel B. The repositioning of the  $\beta$ A strand in AAV2-R432A and the build-up of density at the 2-fold axis are evident. wt-AAV2 is ordered from residue 225, whereas in AAV2-R432A the residues can only be assigned from residue 236 at a resolution of 3.7 Å and from residue 232 at a resolution of 5.0 Å. This density for the ordered N terminus of AAV2-R432A projects into the capsid interior. In wt-AAV2 the VP1/2/3 N termini from 5-fold-related neighboring monomers interact, whereas in AAV2-R432A this interaction is lost (see Fig. 7). The densities in panels A and B are shown at sigma thresholds of 2.5 and 2.0, respectively.

This NGR motif is reportedly essential for integrin  $\alpha 5\beta 1$  coreceptor binding by AAV2 and AAV9 (44, 60). A previous study showed that modification of this motif produced AAV2 capsids that were unable to package genome, and this phenotype was proposed to arise owing to the loss of interaction with residues D431 and R432 (44). The R432A and R513A mutation information suggests that the interactions of residues 511 to 513 and residues 431 to 432 play a critical role in ssDNA genome packaging (44). This implies that the region of the capsid surface lying above these residues serves as a contact point for Rep during the packaging process. The alterations to the AAV2-R432A variant capsid surface above R432 may be responsible for the increased Rep loading reported by Bleker et al. (40). Thus, although a role for residues equivalent to R432 in genome packaging has not been investigated for other AAVs, this residue is critical in AAV2 packaging and thermodynamics, and is predicted to perform a similar role in other AAVs.

DSC experiments provided physical evidence of the decreased stability of the AAV2-R432A with a significantly lower  $T_m$  than wt-AAV2. Prior DSC studies have demonstrated that the specific

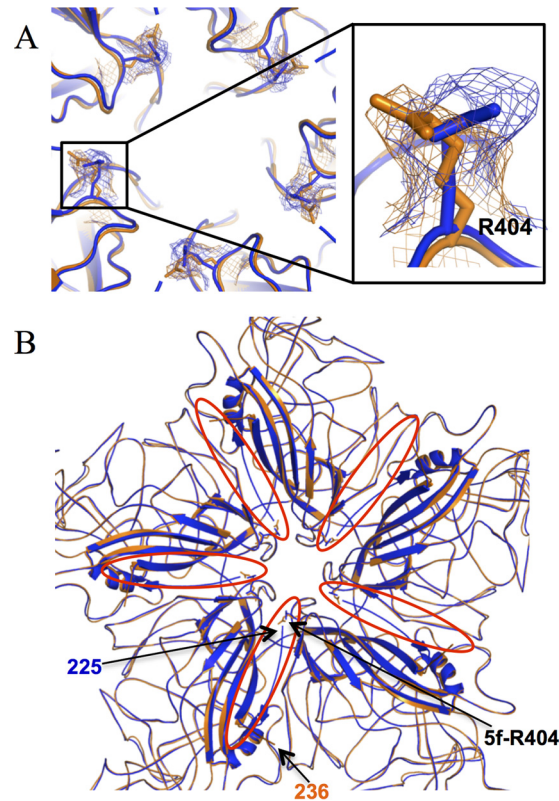


**FIG 7** Wild-type and AAV2-R432A differences at the base of the 5-fold channel. (A) A closeup view of a pentamer of wt-AAV2 (blue ribbon and mesh density) and AAV2-R432A (orange ribbon and mesh density) exhibits the alternative positions of the R404 side chain. The R404 side chain moves away from the opening of the channel in AAV2-R432A. The view is from the interior of the capsid. (B) Pentamer of superposed wt-AAV2 and AAV2-R432A from the capsid interior showing the repositioning of the R404 side chain adjacent to the first ordered N-terminal residue from a 5-fold-related VP monomer in wt-AAV2. The AAV2-R432A structure is disordered up to this position. The density in panel A is shown at a sigma threshold of 2.0.

heat capacity of the AAV capsid directly correlates to its structural stability, and so it follows that a lower  $T_m$  indicates a capsid with decreased stability (59). In addition, the mutant AAV displayed two melting peaks, suggesting dual denaturation events. Of note, the melting profile of AAV8 also demonstrates two transitions, separated by  $\sim 4.3^\circ\text{C}$  (59). A plausible explanation for the AAV2-R432A melting behavior is that two populations of capsids exist, for example, one with altered  $\beta$ A conformation (as observed) and another in transition from the wt-AAV2 conformation. This would explain the lack of or reduced ordering of the altered AAV2-R432A VP N terminus to the same position as for the wt-AAV2 cryo-reconstructed structure despite these residues being within the common VP3 region. Density consistent with the conformational change was seen only at a low sigma threshold ( $0.5\sigma$ ) in the high-resolution map and when resolution was reduced to 5 Å, suggesting a reduced occupancy for the N-terminal amino acids observed beyond position 236. It is also possible that the reduced stability of AAV2-R432A results in dissociation into an intermediate VP oligomeric state such as trimers or pentamers prior to complete capsid disassembly, which appears to be a one step process for AAV2 and other serotypes (59).

In summary, the data reported here suggest that the AAV2



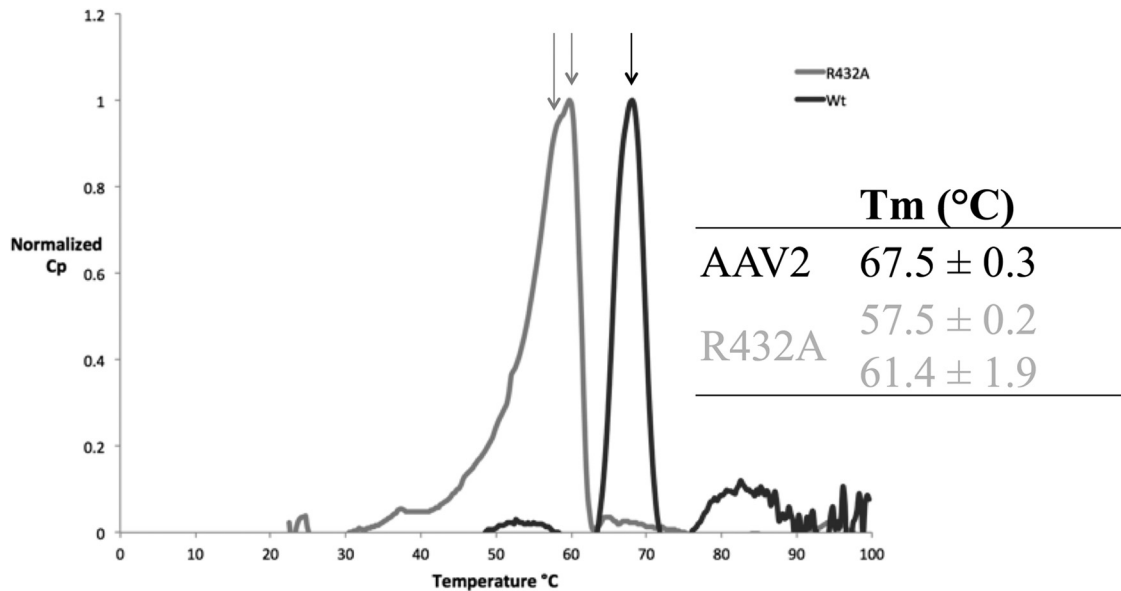


FIG 8 Stability of AAV2 and AAV2-R432A. Melting profile for wt-AAV2 (in black) and AAV2-R432A (in gray). Normalized representations for three experiments are shown.

R432 residue plays an important role in maintaining AAV2 capsid interactions and stability that is important for packaging competency. The loss of contacts between the  $\beta A$  and  $\beta B$  strands below the 5-fold axis would contribute to decreased capsid stability. The 5-fold pore has been suggested to be a site for genome packaging and uncoating from assembled capsids for the AAVs, as well as other parvoviruses. Thus, the structural changes at the base of the 5-fold pore of the AAV2-R432A may contribute to the observed packaging defect. The structural rearrangements observed at the 3-fold region of the AAV2-R432A capsid caused loss of intermonomer interactions which could also lead to global capsid destabilization. The AAV2-R432A structure revealed a buildup of density underneath the 2-fold axis, a process that has been suggested to occur with the VP1/2 common region and VP1u N terminus prior to extrusion through the 5-fold pore (61). This would also suggest that the VP1/2 common region and VP1u are permanently displayed on the capsid surface. However, no density was observed within the 5-fold pore of AAV2-R432A at medium or high resolution. Moreover, density observed at the 2-fold axis was ascribed to residues within the VP1/2/3 common region. The lack of density blocking the pore could merely be a consequence of icosahedral symmetry averaging effects, which diminish the visualization of elements of structure such as VP1u that are present in low copy number. Interestingly, density proximal to the region previously reported to be a nucleotide binding site was observed in wt-AAV2 but not AAV2-R432A, consistent with the inability of the variant to package ssDNA. Finally, the global effect of the single R432A amino change, at a buried capsid location, highlights the plasticity of the assembled capsid and the need to conserve structural fidelity in all functions, including capsid stability and genome packaging.

#### ACKNOWLEDGMENTS

We thank the University of Florida (UF) Interdisciplinary Center for Biotechnology Research (ICBR) electron microscopy lab for providing negative-stain EM services.

Financial support was provided by the UF Division of Sponsored Research and the College of Medicine to establish cryo-EM facilities at the UF ICBR and by the University of California—San Diego (UCSD) and the Agouron Foundation (to T.S.B.) to establish cryo-EM facilities at UCSD. This project was funded in part by NIH R01 GM109524 (M.A.-M., R.M., and N.M.), NIH P01 HL59412 (M.A.-M. and N.M.), NIH R37 GM33050 (T.S.B.), NIH 1S10 RR020016 (T.S.B.), and NIH T32 GM008799 (L.M.D.).

#### FUNDING INFORMATION

This work, including the efforts of Lauren M. Drouin, Bridget Lins, Antonette Bennett, Paul Chipman, Robert McKenna, Weijun Chen, Nicholas Muzyczka, and Mavis Agbandje-McKenna, was funded by HHS | National Institutes of Health (NIH) (GM109524 and HL59412). This work, including the efforts of Maria Janssen, Giovanni Cardone, and Timothy S. Baker, was funded by HHS | National Institutes of Health (NIH) (GM33050). This work, including the efforts of Lauren M. Drouin, was funded by HHS | National Institutes of Health (NIH) (GM008799).

#### REFERENCES

- Asokan A, Schaffer DV, Samulski RJ. 2012. The AAV vector toolkit: poised at the clinical crossroads. *Mol Ther* 20:699–708. <http://dx.doi.org/10.1038/mt.2011.287>.
- Daya S, Berns KI. 2008. Gene therapy using adeno-associated virus vectors. *Clin Microbiol Rev* 21:583–593. <http://dx.doi.org/10.1128/CMR.00008-08>.
- Flotte TR, Carter BJ. 1995. Adeno-associated virus vectors for gene therapy. *Gene Ther* 2:357–362.
- Chapman M, Agbandje-McKenna M. 2006. Atomic structure of viral particles, p 107–123. *In* Kerr CS, Jr, Bloom ME, Linden RM, Parrish CR (ed), *Parvoviruses*. Edward Arnold, Ltd, New York, NY.
- Grieger JC, Johnson JS, Gurda-Whitaker B, Agbandje-McKenna M, Samulski RJ. 2007. Surface-exposed adeno-associated virus Vp1-NLS capsid fusion protein rescues infectivity of noninfectious wild-type Vp2/Vp3 and Vp3-only capsids but not that of fivefold pore mutant virions. *J Virol* 81:7833–7843. <http://dx.doi.org/10.1128/JVI.00580-07>.
- Bleker S, Sonntag F, Kleinschmidt JA. 2005. Mutational analysis of narrow pores at the fivefold symmetry axes of adeno-associated virus type 2 capsids reveals a dual role in genome packaging and activation of phospholipase A2 activity. *J Virol* 79:2528–2540. <http://dx.doi.org/10.1128/JVI.79.4.2528-2540.2005>.

7. Buller RM, Rose JA. 1978. Characterization of adenovirus-associated virus-induced polypeptides in KB cells. *J Virol* 25:331–338.
8. Rose JA, Maizel JV, Jr, Inman JK, Shatkin AJ. 1971. Structural proteins of adenovirus-associated viruses. *J Virol* 8:766–770.
9. Johnson FB, Ozer HL, Hoggan MD. 1971. Structural proteins of adenovirus-associated virus type 3. *J Virol* 8:860–863.
10. Snijder J, van de Waterbeemd M, Damoc E, Denisov E, Grinfeld D, Bennett A, Agbandje-McKenna M, Makarov A, Heck AJ. 2014. Defining the stoichiometry and cargo load of viral and bacterial nanoparticles by Orbitrap mass spectrometry. *J Am Chem Soc* 136:7295–7299. <http://dx.doi.org/10.1021/ja502616y>.
11. Sonntag F, Schmidt K, Kleinschmidt JA. 2010. A viral assembly factor promotes AAV2 capsid formation in the nucleolus. *Proc Natl Acad Sci U S A* 107:10220–10225. <http://dx.doi.org/10.1073/pnas.1001673107>.
12. Sonntag F, Kother K, Schmidt K, Weghofer M, Raupp C, Nieto K, Kuck A, Gerlach B, Bottcher B, Muller OJ, Lux K, Horer M, Kleinschmidt JA. 2011. The assembly-activating protein promotes capsid assembly of different adeno-associated virus serotypes. *J Virol* 85:12686–12697. <http://dx.doi.org/10.1128/JVI.05359-11>.
13. Naumer M, Sonntag F, Schmidt K, Nieto K, Panke C, Davey NE, Popa-Wagner R, Kleinschmidt JA. 2012. Properties of the adeno-associated virus assembly-activating protein. *J Virol* 86:13038–13048. <http://dx.doi.org/10.1128/JVI.01675-12>.
14. DiMattia MA, Nam HJ, Van Vliet K, Mitchell M, Bennett A, Gurda BL, McKenna R, Olson NH, Sinkovits RS, Potter M, Byrne BJ, Aslanidi G, Zolotukhin S, Muzyczka N, Baker TS, Agbandje-McKenna M. 2012. Structural insight into the unique properties of adeno-associated virus serotype 9. *J Virol* 86:6947–6958. <http://dx.doi.org/10.1128/JVI.07232-11>.
15. Govindasamy L, Dimattia MA, Gurda BL, Halder S, McKenna R, Chiorini JA, Muzyczka N, Zolotukhin S, Agbandje-McKenna M. 2013. Structural insights into adeno-associated virus serotype 5. *J Virol* 87:11187–11199. <http://dx.doi.org/10.1128/JVI.00867-13>.
16. Govindasamy L, Padron E, McKenna R, Muzyczka N, Kaludov N, Chiorini JA, Agbandje-McKenna M. 2006. Structurally mapping the diverse phenotype of adeno-associated virus serotype 4. *J Virol* 80:11556–11570. <http://dx.doi.org/10.1128/JVI.01536-06>.
17. Kronenberg S, Kleinschmidt JA, Bottcher B. 2001. Electron cryo-microscopy and image reconstruction of adeno-associated virus type 2 empty capsids. *EMBO Rep* 2:997–1002. <http://dx.doi.org/10.1093/embo-reports/kve234>.
18. Lerch TF, Xie Q, Chapman MS. 2010. The structure of adeno-associated virus serotype 3B (AAV-3B): insights into receptor binding and immune evasion. *Virology* 403:26–36. <http://dx.doi.org/10.1016/j.virol.2010.03.027>.
19. Nam HJ, Gurda BL, McKenna R, Potter M, Byrne B, Salganik M, Muzyczka N, Agbandje-McKenna M. 2011. Structural studies of adeno-associated virus serotype 8 capsid transitions associated with endosomal trafficking. *J Virol* 85:11791–11799. <http://dx.doi.org/10.1128/JVI.05305-11>.
20. Nam HJ, Lane MD, Padron E, Gurda B, McKenna R, Kohlbrenner E, Aslanidi G, Byrne B, Muzyczka N, Zolotukhin S, Agbandje-McKenna M. 2007. Structure of adeno-associated virus serotype 8, a gene therapy vector. *J Virol* 81:12260–12271. <http://dx.doi.org/10.1128/JVI.01304-07>.
21. Ng R, Govindasamy L, Gurda BL, McKenna R, Kozyreva OG, Samulski RJ, Parent KN, Baker TS, Agbandje-McKenna M. 2010. Structural characterization of the dual glycan binding adeno-associated virus serotype 6. *J Virol* 84:12945–12957. <http://dx.doi.org/10.1128/JVI.01235-10>.
22. Xie Q, Bu W, Bhatia S, Hare J, Somasundaram T, Azzi A, Chapman MS. 2002. The atomic structure of adeno-associated virus (AAV-2), a vector for human gene therapy. *Proc Natl Acad Sci U S A* 99:10405–10410. <http://dx.doi.org/10.1073/pnas.162250899>.
23. Xie Q, Lerch TF, Meyer NL, Chapman MS. 2011. Structure-function analysis of receptor-binding in adeno-associated virus serotype 6 (AAV-6). *Virology* 420:10–19. <http://dx.doi.org/10.1016/j.virol.2011.08.011>.
24. McCraw DM, O'Donnell JK, Taylor KA, Stagg SM, Chapman MS. 2012. Structure of adeno-associated virus-2 in complex with neutralizing monoclonal antibody A20. *Virology* 431:40–49. <http://dx.doi.org/10.1016/j.virol.2012.05.004>.
25. Gurda BL, DiMattia MA, Miller EB, Bennett A, McKenna R, Weichert WS, Nelson CD, Chen WJ, Muzyczka N, Olson NH, Sinkovits RS, Chiorini JA, Zolotukhin S, Kozyreva OG, Samulski RJ, Baker TS, Parrish CR, Agbandje-McKenna M. 2013. Capsid antibodies to different adeno-associated virus serotypes bind common regions. *J Virol* 87:9111–9124. <http://dx.doi.org/10.1128/JVI.00622-13>.
26. Gurda BL, Raupp C, Popa-Wagner R, Naumer M, Olson NH, Ng R, McKenna R, Baker TS, Kleinschmidt JA, Agbandje-McKenna M. 2012. Mapping a neutralizing epitope onto the capsid of adeno-associated virus serotype 8. *J Virol* 86:7739–7751. <http://dx.doi.org/10.1128/JVI.00218-12>.
27. Kern A, Schmidt K, Leder C, Muller OJ, Wobus CE, Bettinger K, Von der Lieth CW, King JA, Kleinschmidt JA. 2003. Identification of a heparin-binding motif on adeno-associated virus type 2 capsids. *J Virol* 77:11072–11081. <http://dx.doi.org/10.1128/JVI.77.20.11072-11081.2003>.
28. Levy HC, Bowman VD, Govindasamy L, McKenna R, Nash K, Warrington K, Chen W, Muzyczka N, Yan X, Baker TS, Agbandje-McKenna M. 2009. Heparin binding induces conformational changes in adeno-associated virus serotype 2. *J Struct Biol* 165:146–156. <http://dx.doi.org/10.1016/j.jsb.2008.12.002>.
29. Lochrie MA, Tatsuno GP, Christie B, McDonnell JW, Zhou S, Surosky R, Pierce GF, Colosi P. 2006. Mutations on the external surfaces of adeno-associated virus type 2 capsids that affect transduction and neutralization. *J Virol* 80:821–834. <http://dx.doi.org/10.1128/JVI.80.2.821-834.2006>.
30. O'Donnell J, Taylor KA, Chapman MS. 2009. Adeno-associated virus-2 and its primary cellular receptor-cryo-EM structure of a heparin complex. *Virology* 385:434–443. <http://dx.doi.org/10.1016/j.virol.2008.11.037>.
31. Opie SR, Warrington KH, Jr, Agbandje-McKenna M, Zolotukhin S, Muzyczka N. 2003. Identification of amino acid residues in the capsid proteins of adeno-associated virus type 2 that contribute to heparan sulfate proteoglycan binding. *J Virol* 77:6995–7006. <http://dx.doi.org/10.1128/JVI.77.12.6995-7006.2003>.
32. Tseng YS, Gurda BL, Chipman P, McKenna R, Afione S, Chiorini JA, Muzyczka N, Olson NH, Baker TS, Kleinschmidt J, Agbandje-McKenna M. 2015. Adeno-associated virus serotype 1 (AAV1)- and AAV5-antibody complex structures reveal evolutionary commonalities in parvovirus antigenic reactivity. *J Virol* 89:1794–1808. <http://dx.doi.org/10.1128/JVI.02710-14>.
33. Wobus CE, Hugle-Dorr B, Girod A, Petersen G, Hallek M, Kleinschmidt JA. 2000. Monoclonal antibodies against the adeno-associated virus type 2 (AAV-2) capsid: epitope mapping and identification of capsid domains involved in AAV-2-cell interaction and neutralization of AAV-2 infection. *J Virol* 74:9281–9293. <http://dx.doi.org/10.1128/JVI.74.19.9281-9293.2000>.
34. Wu P, Xiao W, Conlon T, Hughes J, Agbandje-McKenna M, Ferkol T, Flotte T, Muzyczka N. 2000. Mutational analysis of the adeno-associated virus type 2 (AAV2) capsid gene and construction of AAV2 vectors with altered tropism. *J Virol* 74:8635–8647. <http://dx.doi.org/10.1128/JVI.74.18.8635-8647.2000>.
35. King JA, Dubielzig R, Grimm D, Kleinschmidt JA. 2001. DNA helicase-mediated packaging of adeno-associated virus type 2 genomes into preformed capsids. *EMBO J* 20:3282–3291. <http://dx.doi.org/10.1093/emboj/20.12.3282>.
36. Chiorini JA, Wiener SM, Owens RA, Kyostio SR, Kotin RM, Safer B. 1994. Sequence requirements for stable binding and function of Rep68 on the adeno-associated virus type 2 inverted terminal repeats. *J Virol* 68:7448–7457.
37. Chiorini JA, Yang L, Safer B, Kotin RM. 1995. Determination of adeno-associated virus Rep68 and Rep78 binding sites by random sequence oligonucleotide selection. *J Virol* 69:7334–7338.
38. Im DS, Muzyczka N. 1990. The AAV origin binding protein Rep68 is an ATP-dependent site-specific endonuclease with DNA helicase activity. *Cell* 61:447–457. [http://dx.doi.org/10.1016/0092-8674\(90\)90526-K](http://dx.doi.org/10.1016/0092-8674(90)90526-K).
39. Kyostio SR, Wonderling RS, Owens RA. 1995. Negative regulation of the adeno-associated virus (AAV) P5 promoter involves both the P5 rep binding site and the consensus ATP-binding motif of the AAV Rep68 protein. *J Virol* 69:6787–6796.
40. Bleker S, Pawlita M, Kleinschmidt JA. 2006. Impact of capsid conformation and Rep-capsid interactions on adeno-associated virus type 2 genome packaging. *J Virol* 80:810–820. <http://dx.doi.org/10.1128/JVI.80.2.810-820.2006>.
41. Plevka P, Hafenstein S, Li L, D'Abbramo A, Jr, Cotmore SF, Rossmann MG, Tattersall P. 2011. Structure of a packaging-defective mutant of minute virus of mice indicates that the genome is packaged via a pore at a 5-fold axis. *J Virol* 85:4822–4827. <http://dx.doi.org/10.1128/JVI.02598-10>.

42. Warrington KH, Jr, Gorbatyuk OS, Harrison JK, Opie SR, Zolotukhin S, Muzyczka N. 2004. Adeno-associated virus type 2 VP2 capsid protein is nonessential and can tolerate large peptide insertions at its N terminus. *J Virol* 78:6595–6609. <http://dx.doi.org/10.1128/JVI.78.12.6595-6609.2004>.
43. Lux K, Goerlitz N, Schlemminger S, Perabo L, Goldnau D, Endell J, Leike K, Kofler DM, Finke S, Hallek M, Buning H. 2005. Green fluorescent protein-tagged adeno-associated virus particles allow the study of cytosolic and nuclear trafficking. *J Virol* 79:11776–11787. <http://dx.doi.org/10.1128/JVI.79.18.11776-11787.2005>.
44. Asokan A, Hamra JB, Govindasamy L, Agbandje-McKenna M, Samulski RJ. 2006. Adeno-associated virus type 2 contains an integrin alpha5beta1 binding domain essential for viral cell entry. *J Virol* 80:8961–8969. <http://dx.doi.org/10.1128/JVI.00843-06>.
45. Kohlbrenner E, Aslanidi G, Nash K, Shklyayev S, Campbell-Thompson M, Byrne BJ, Snyder RO, Muzyczka N, Warrington KH, Zolotukhin S. 2005. Successful production of pseudotyped rAAV vectors using a modified baculovirus expression system. *Mol Ther* 12:1217–1225.
46. Mindell JA, Grigorieff N. 2003. Accurate determination of local defocus and specimen tilt in electron microscopy. *J Struct Biol* 142:334–347. [http://dx.doi.org/10.1016/S1047-8477\(03\)00069-8](http://dx.doi.org/10.1016/S1047-8477(03)00069-8).
47. Yan X, Sinkovits RS, Baker TS. 2007. AUTO3DEM: an automated and high-throughput program for image reconstruction of icosahedral particles. *J Struct Biol* 157:73–82. <http://dx.doi.org/10.1016/j.jsb.2006.08.007>.
48. Baker TS, Olson NH, Fuller SD. 1999. Adding the third dimension to virus life cycles: three-dimensional reconstruction of icosahedral viruses from cryo-electron micrographs. *Microbiol Mol Biol Rev* 63:862–922.
49. Yan X, Dryden KA, Tang J, Baker TS. 2007. Ab initio random model method facilitates 3D reconstruction of icosahedral particles. *J Struct Biol* 157:211–225. <http://dx.doi.org/10.1016/j.jsb.2006.07.013>.
50. Rosenthal PB, Henderson R. 2003. Optimal determination of particle orientation, absolute hand, and contrast loss in single-particle electron cryomicroscopy. *J Mol Biol* 333:721–745. <http://dx.doi.org/10.1016/j.jmb.2003.07.013>.
51. Havelka WA, Henderson R, Oesterhelt D. 1995. Three-dimensional structure of halorhodopsin at 7-Å resolution. *J Mol Biol* 247:726–738. [http://dx.doi.org/10.1016/S0022-2836\(05\)80151-2](http://dx.doi.org/10.1016/S0022-2836(05)80151-2).
52. Carrillo-Tripp M, Shepherd CM, Borelli IA, Venkataraman S, Lander G, Natarajan P, Johnson JE, Brooks CL, III, Reddy VS. 2009. VIPERdb2: an enhanced and web API enabled relational database for structural virology. *Nucleic Acids Res* 37:D436–D442. <http://dx.doi.org/10.1093/nar/gkn840>.
53. Pettersen EF, Goddard TD, Huang CC, Couch GS, Greenblatt DM, Meng EC, Ferrin TE. 2004. UCSF Chimera: a visualization system for exploratory research and analysis. *J Comput Chem* 25:1605–1612. <http://dx.doi.org/10.1002/jcc.20084>.
54. Emsley P, Cowtan K. 2004. Coot: model-building tools for molecular graphics. *Acta Crystallogr D Biol Crystallogr* 60:2126–2132. <http://dx.doi.org/10.1107/S0907444904019158>.
55. Adams PD, Afonine PV, Bunkoczi G, Chen VB, Davis IW, Echols N, Headd JJ, Hung LW, Kapral GJ, Grosse-Kunstleve RW, McCoy AJ, Moriarty NW, Oeffner R, Read RJ, Richardson DC, Richardson JS, Terwilliger TC, Zwart PH. 2010. PHENIX: a comprehensive Python-based system for macromolecular structure solution. *Acta Crystallogr D Biol Crystallogr* 66:213–221. <http://dx.doi.org/10.1107/S0907444909052925>.
56. DeLano WL. 2008. The PyMOL molecular graphics system. DeLano Scientific LLC, New York, NY. <http://www.pymol.org>.
57. Halder S, Ng R, Agbandje-McKenna M. 2012. Parvoviruses: structure and infection. *Future Virol* 7:253–278. <http://dx.doi.org/10.2217/fvl.12.12>.
58. Halder S, Van Vliet K, Smith JK, Duong TT, McKenna R, Wilson JM, Agbandje-McKenna M. 2015. Structure of neurotropic adeno-associated virus AAVrh.8. *J Struct Biol* 192:21–36. <http://dx.doi.org/10.1016/j.jsb.2015.08.017>.
59. Rayaprolu V, Kruse S, Kant R, Venkatakrishnan B, Movahed N, Brooke D, Lins B, Bennett A, Potter T, McKenna R, Agbandje-McKenna M, Bothner B. 2013. Comparative analysis of adeno-associated virus capsid stability and dynamics. *J Virol* <http://dx.doi.org/10.1128/JVI.01415-13>.
60. Shen S, Berry GE, Castellanos Rivera RM, Cheung RY, Troupes AN, Brown SM, Kafri T, Asokan A. 2015. Functional analysis of the putative integrin recognition motif on adeno-associated virus 9. *J Biol Chem* 290:1496–1504. <http://dx.doi.org/10.1074/jbc.M114.608281>.
61. Kronenberg S, Bottcher B, von der Lieth CW, Bleker S, Kleinschmidt JA. 2005. A conformational change in the adeno-associated virus type 2 capsid leads to the exposure of hidden VP1 N termini. *J Virol* 79:5296–5303. <http://dx.doi.org/10.1128/JVI.79.9.5296-5303.2005>.